# **Green Chemistry**



View Article Online

### PAPER

( Check for updates

Cite this: Green Chem., 2020, 22, 7552

Received 20th August 2020, Accepted 29th September 2020 DOI: 10.1039/d0gc02836c

rsc.li/greenchem

### Introduction

The rapidly growing consumption of fossil fuels with excessive emission of CO<sub>2</sub> has been contributing to the severe global warming problem and the potential energy shortage.<sup>1,2</sup> Utilizing solar energy to convert CO<sub>2</sub> into fuels provides a promising approach to solving the above problems, and scientists have devoted tremendous attention to developing various photocatalysts for CO<sub>2</sub> reduction.<sup>3-9</sup> Recently, graphitic carbon nitride (g-C<sub>3</sub>N<sub>4</sub>)-supported single-atomic site catalysts have emerged as remarkable photocatalysts.<sup>10-13</sup> By virtue of the lone pair electrons, the N atoms in the framework can capture various transition metal ions, thus forming single-atomic metal sites on g-C<sub>3</sub>N<sub>4</sub>. In addition, the charge densities of the coordinated metal atoms would be altered by the neighboring N atoms, which may in turn change the adsorption strength and reaction barriers. Density functional theory (DFT) calculations have suggested that single-atomic Pd or Pt loaded on g-C<sub>3</sub>N<sub>4</sub> can act as effective catalytic sites for photocatalytic CO<sub>2</sub>

School of Materials Science & Engineering, Tianjin University of Technology, Tianjin 300384, China. E-mail: yli@email.tjut.edu.cn, lutongbu@tjut.edu.cn

## Integrating Z-scheme heterojunction of Co<sub>1</sub>-C<sub>3</sub>N<sub>4</sub>@ $\alpha$ -Fe<sub>2</sub>O<sub>3</sub> for efficient visible-light-driven photocatalytic CO<sub>2</sub> reduction<sup>†</sup>

Bing-Cai He, Chao Zhang, Pei-Pei Luo, Yu Li 🕩 \* and Tong-Bu Lu 🕩 \*

Photocatalytic CO<sub>2</sub> reduction coupled with water oxidation provides a fascinating approach to mitigating the issues of global warming and energy shortage. Herein, a direct Z-scheme heterojunction of Co<sub>1</sub>-C<sub>3</sub>N<sub>4</sub>( $\alpha$ -Fe<sub>2</sub>O<sub>3</sub> comprising a g-C<sub>3</sub>N<sub>4</sub>-supported single-atomic Co site catalyst (denoted as Co<sub>1</sub>-C<sub>3</sub>N<sub>4</sub>) and  $\alpha$ -Fe<sub>2</sub>O<sub>3</sub> nanorod arrays is fabricated for efficient CO<sub>2</sub> reduction. A CO production rate of 14.9 µmol g<sup>-1</sup> h<sup>-1</sup> with a high CO selectivity (>99%) is achieved under visible-light irradiation without any sacrificial agents other than water. Time-resolved photoluminescence (TRPL) analysis reveals that both the Z-scheme mechanism and the single-atomic Co sites contribute to the prolonged lifetime of the photoinduced excitons. Moreover, the formation of the Z-scheme heterojunction would lead to an altered charge density of the single-atomic Co sites. *In situ* diffuse reflectance infrared Fourier-transform spectroscopy and anion adsorption measurements reveal that the key intermediate CO<sub>2</sub><sup>-</sup> could be efficiently stabilized by the positively charged Co sites in Co<sub>1</sub>-C<sub>3</sub>N<sub>4</sub>@ $\alpha$ -Fe<sub>2</sub>O<sub>3</sub>, thus enhancing the CO<sub>2</sub> reduction performance. This work offers a new direction for the rational design of single-atomic site catalysts in artificial photosynthesis.

> reduction, leading to two different preferential products, HCOOH and CH<sub>4</sub>, respectively.<sup>14</sup> With the aid of triethylamine (TEA), single-atomic  $Co^{2+}$  sites on  $C_3N_4$  with different loadings have been successfully synthesized, and the optimized sample with a cobalt loading of 0.128  $\mu mol\ mg^{-1}$  exhibits a CO production rate of approximately 25.5 µmol g<sup>-1</sup> h<sup>-1</sup> under 60 mW  $cm^{-2}$  incident light in the presence of triethanolamine (TEOA) as a sacrificial electron donor.<sup>15</sup> Recently, we have developed an efficient photocatalyst for CO2 reduction by implanting single titanium oxide species on g-C<sub>3</sub>N<sub>4</sub>.<sup>16</sup> In the presence of the Co(bpy)<sub>3</sub>Cl<sub>2</sub> co-catalyst and TEOA, a CO production rate of 283.9  $\mu$ mol g<sup>-1</sup> h<sup>-1</sup> has been achieved under visible light irradiation. These results strongly demonstrate the viability of g-C<sub>3</sub>N<sub>4</sub>-supported single-atomic site catalysts for photocatalytic CO2 reduction. However, the use of TEOA makes these catalysts less attractive since TEOA is much more expensive than CO. Therefore, it still remains a great challenge to develop low-cost and robust g-C<sub>3</sub>N<sub>4</sub>-based photocatalysts with high efficiency for CO<sub>2</sub> conversion using water as an electron source.

> Owing to the wide band gap (~2.7 eV), g-C<sub>3</sub>N<sub>4</sub> can only utilize a marginal portion of visible light ( $\lambda$  < 460 nm).<sup>17</sup> Moreover, the water oxidation capacity of g-C<sub>3</sub>N<sub>4</sub> is poor due to the high energy level of the valence band.<sup>18–20</sup> In this situation, integrating g-C<sub>3</sub>N<sub>4</sub> with an appropriate semiconductor possessing a narrower band gap and a more positive valence band to establish a Z-scheme heterojunction has been acknowledged

MOE International Joint Laboratory of Materials Microstructure,

Institute for New Energy Materials and Low Carbon Technologies,

<sup>†</sup>Electronic supplementary information (ESI) available. See DOI: 10.1039/ d0gc02836c

as an effective strategy, because the Z-scheme heterojunction not only facilitates the spatial separation of the photo-induced electron-hole pairs, but also preserves the maximum capacities for reduction and oxidation of the composites.<sup>20–23</sup>

Herein, we construct a direct Z-scheme heterojunction of Co<sub>1</sub>-C<sub>3</sub>N<sub>4</sub>(aα-Fe<sub>2</sub>O<sub>3</sub>, which composes by single-atomic Co sites loaded on g-C<sub>3</sub>N<sub>4</sub> (Co<sub>1</sub>-C<sub>3</sub>N<sub>4</sub>) integrated with  $\alpha$ -Fe<sub>2</sub>O<sub>3</sub> nanorod arrays, for efficient visible-light-driven CO<sub>2</sub> reduction coupled with water oxidation. The light-absorption range of Co<sub>1</sub>-C<sub>3</sub>N<sub>4</sub> is greatly extended to the entire visible-light region and the lifetime of photo-induced charge carriers is significantly prolonged by the successful incorporation of  $\alpha$ -Fe<sub>2</sub>O<sub>3</sub>. Moreover, benefiting from the charge transfer induced by the different Fermi levels between  $\alpha$ -Fe<sub>2</sub>O<sub>3</sub> and Co<sub>1</sub>-C<sub>3</sub>N<sub>4</sub>, the charge density of single-atomic Co can be further regulated. The results of anion adsorption measurements imply that the stabilization of the critical intermediate  $CO_2^-$  is more efficient on the singleatomic Co sites with a higher positive charge. Compared with Co<sub>1</sub>-C<sub>3</sub>N<sub>4</sub>, the constructed Z-scheme heterojunction shows a substantial improvement for photocatalytic CO2 conversion to CO, with 2.8 times higher than that of Co<sub>1</sub>-C<sub>3</sub>N<sub>4</sub> under visible light irradiation and almost 100% CO selectivity.

### Experimental

#### Materials

FeCl<sub>3</sub>·6H<sub>2</sub>O (99%, AR) and CoCl<sub>2</sub>·6H<sub>2</sub>O (99%, AR) were purchased from Aladdin. Urea (99%, AR), NaOH (96%, AR) and Na<sub>2</sub>SO<sub>4</sub> (99%, AR) were purchased from FuChen Chemical Reagent Factory. Nafion 117 solution (~5% in alcohol/water) was purchased from Sigma-Aldrich. CO<sub>2</sub> (99.999%) and Ar (99.999%) were purchased from Tianjin Huanyu Gas company. <sup>13</sup>CO<sub>2</sub> (99%) was purchased from Sigma-Aldrich and H<sub>2</sub><sup>18</sup>O (99%) was purchased from Energy Chemical. All chemicals were used as received without further purification. The ultrapure water (Milli-Q water) with an electrical resistivity of 18.2 MΩ cm was used in all experiments.

#### Synthetic procedures

The α-Fe2O3 nanorod arrays were fabricated by a modified strategy reported previously.<sup>24,25</sup> In brief, a piece of fluorinedoped tin oxide (FTO) glass (1 cm × 2.5 cm) was sonicated in acetone, ethanol and water, respectively. Then the FTO glass was leant on the inner side of a Teflon liner with the FTO side facing down. Subsequently, an aqueous solution (15 mL) containing FeCl<sub>3</sub>·6H<sub>2</sub>O (0.51 g) and urea (0.17 g) was added, and the liner was sealed in a stainless steel autoclave, and then heated at 100 °C for 4 h. The as-prepared sample was washed with water and dried by N2 flow to remove redundant sediment. The film was annealed at 550 °C for 2 h and subsequently at 660 °C for 20 min in a muffle furnace with a ramping rate of 2 °C min<sup>-1</sup>, and the  $\alpha$ -Fe<sub>2</sub>O<sub>3</sub> nanorod arrays were finally obtained. The loading amount of the  $\alpha$ -Fe<sub>2</sub>O<sub>3</sub> nanorod arrays was determined to be 0.3 mg by weighing the FTO glass before and after the synthesis.

The g-C<sub>3</sub>N<sub>4</sub>-supported Co single-atom catalyst was prepared by using a two-step strategy.<sup>26</sup> Specifically, urea (15 g) was put into a crucible with a cover, and calcined at 550 °C for 4 h with a ramping rate of 10 °C min<sup>-1</sup>. After cooling down naturally, the product was heated again at 500 °C for 2 h to obtain exfoliated g-C<sub>3</sub>N<sub>4</sub>. For the synthesis of g-C<sub>3</sub>N<sub>4</sub>-supported singleatomic Co site catalyst (Co1-C3N4), g-C3N4 (10 mg) was well dispersed in water (10 mL) by vigorous sonication for 30 min. Next, an aqueous solution (500  $\mu$ L) containing CoCl<sub>2</sub>·6H<sub>2</sub>O (0.336 mM) was dropped into the g-C<sub>3</sub>N<sub>4</sub> suspension under magnetic stirring. Subsequently, the suspension was stirred for 12 h at 80 °C in an oil bath. The above mixture was then frozen by liquid nitrogen and further dried in vacuum for 48 h by using a lyophilizer. The obtained sample was placed in a porcelain boat and heated to 400 °C for 2 h with a ramping rate of 5 °C min<sup>-1</sup> under Ar atmosphere. Similar procedures were applied for the synthesis of the g-C<sub>3</sub>N<sub>4</sub>-supported CoO nanoparticle catalyst (CoNP-C3N4), except that the concentration of CoCl<sub>2</sub>·6H<sub>2</sub>O was increased to 3.36 mM.

To fabricate the Z-scheme system, a well-dispersed aqueous suspension (300  $\mu$ L) of Co<sub>1</sub>-C<sub>3</sub>N<sub>4</sub> (1 mg mL<sup>-1</sup>, 0.3 mg in total) was first drop-coated onto the  $\alpha$ -Fe<sub>2</sub>O<sub>3</sub> nanorod arrays under 60 °C. To strengthen the contact between  $\alpha$ -Fe<sub>2</sub>O<sub>3</sub> and Co<sub>1</sub>-C<sub>3</sub>N<sub>4</sub>, the sample was transferred to a tube furnace and calcined at 200 °C for 2 h, with a ramping rate of 5 °C min<sup>-1</sup> under Ar atmosphere. The obtained sample was denoted as Co<sub>1</sub>-C<sub>3</sub>N<sub>4</sub>@ $\alpha$ -Fe<sub>2</sub>O<sub>3</sub>. C<sub>3</sub>N<sub>4</sub>@ $\alpha$ -Fe<sub>2</sub>O<sub>3</sub> and CoNP-C<sub>3</sub>N<sub>4</sub>@ $\alpha$ -Fe<sub>2</sub>O<sub>3</sub> were fabricated according to the same method as that of Co<sub>1</sub>-C<sub>3</sub>N<sub>4</sub>@ $\alpha$ -Fe<sub>2</sub>O<sub>3</sub>, except that Co<sub>1</sub>-C<sub>3</sub>N<sub>4</sub> was replaced by g-C<sub>3</sub>N<sub>4</sub> and CoNP-C<sub>3</sub>N<sub>4</sub>, respectively.

#### Characterization

The powder X-ray diffraction (XRD) patterns were recorded by using a Rigaku SmartLab 9 kW with Cu-Ka radiation ( $\lambda$  = 1.5418 Å). A Thermo scientific iCAP RQ inductively coupled plasma-mass spectrometer (ICP-MS) was used to determine the Co content. Scanning electron microscopy (SEM) was performed using a FEI Verios 460L scanning electron microscope. Transmission electron microscopy (TEM) images and High-Resolution Transmission Electron Microscopy (HRTEM) images were obtained on FEI Tecnai G2 Spirit Twin and FEI Talos F200X transmission electron microscopes, respectively. Atomic-resolution aberration-corrected high-angle annular scanning transmission electron microscopy dark-field (HAADF-STEM) images and elemental mapping were obtained by using a FEI Titan Themis Cubed G2 60-300 transmission electron microscope. X-ray photoelectron spectroscopy (XPS) measurements were carried out by using a Thermo Scientific ESCALAB250Xi photoelectron spectrometer equipped with Mg Kα (1253.6 eV) as the X-ray source. Ultraviolet-visible (UV-vis) spectroscopic measurements were performed by using a PerkinElmer Lambda 750 UV/VIS/NIR spectrometer. A PerkinElmer Frontier Mid-IR FTIR spectrometer was employed to obtain Fourier-transform infrared spectra. The steady-state photoluminescence spectra (PL) were recorded on a Hitachi F-4600 fluorescence spectrometer. The time-resolved photo-

#### Paper

luminescence (TRPL) curves were recorded using a PicoQuant MicroTime 200 time-resolved confocal fluorescence instrument. The electron spin resonance (ESR) analysis was conducted on an electron paramagnetic resonance spectrometer (Bruker EMXplus-6/1) with 5,5-dimethyl-1-pyrroline *N*-oxide (DMPO) as the trapping agent at 298 K. CO<sub>2</sub> adsorption was tested by using a MicrotracBEL BELSORP-Max gas adsorption instrument at 298 K. A Hansatech Chlorolab-2 liquid-phase oxygen measurement system was employed to detect the oxygen evolution during the photocatalytic CO<sub>2</sub> reduction.

#### Photocatalytic CO<sub>2</sub> reduction measurements

Photocatalytic CO<sub>2</sub> reduction tests were conducted in a gassolid setup. A piece of the sample was placed in a 35 mL quartz tube. High-purity CO<sub>2</sub> (99.999%) was first passed through water to carry H<sub>2</sub>O vapor and then introduced into the quartz tube. The quartz tube was purged with the CO<sub>2</sub>/H<sub>2</sub>O gas mixture for 30 min and sealed by using a rubber stopper. A 300 W xenon lamp (CEL-HXF300, CEAULIGHT) with a 400 nm cutoff filter was positioned above the sample as the light source. Gaseous products (CO, CH<sub>4</sub>, and H<sub>2</sub>) were analysed by using a SHIMADZU GC-2014 gas chromatograph equipped with TCD and FID dual detectors. The products of the <sup>13</sup>CO<sub>2</sub> and H<sub>2</sub><sup>18</sup>O isotopic experiments were analysed by using a Hiden Analytical HPR20 mass spectrometer.

#### Photoelectrochemical measurements

All measurements were performed on a CHI 760E electrochemical workstation with a three-electrode setup (working electrode: FTO glass-supported sample; reference electrode: Ag/AgCl electrode; counter electrode: Pt foil) in 0.1 M Na<sub>2</sub>SO<sub>4</sub> aqueous solution. To measure the photo-current responses, a 300 W Xe lamp (CEL-HXF300, CEAULIGHT) with a 400 nm cutoff filter was used as the light source. A potential of 0.5 V *vs.* Ag/AgCl was applied on the sample and the light was chopped every 10 s to simulate light/dark conditions during the test. Electrochemical impedance spectroscopy (EIS) was carried out in the frequency range of 0.1 MHz to 0.1 Hz with an AC voltage amplitude of 5 mV at an open-circuit potential under visible-light irradiation with a power density of 200 mW cm<sup>-2</sup>.

#### In situ DRIFTS characterization

In situ diffuse reflectance infrared Fourier-transform spectra (DRIFTS) were recorded on a Bruker IFS 66v Fourier-transform spectrometer at the Infrared Spectroscopy and Microspectroscopy Endstation (BL01B) in the National Synchrotron Radiation Laboratory (NSRL), Hefei.<sup>27</sup> The sample was placed in a Harrick diffuse reflectance reaction chamber fixed in the light path. The chamber was equipped with two ZnSe windows and two gas channels. Each spectrum was recorded by 128 scans with a resolution of 4 cm<sup>-1</sup>. The spectrum recorded under Ar atmosphere was set as the background signal.

### Results and discussion

The composite structure comprising  $\alpha$ -Fe<sub>2</sub>O<sub>3</sub> and Co<sub>1</sub>-C<sub>3</sub>N<sub>4</sub> was fabricated by a multi-step strategy (Fig. 1a). Co<sub>1</sub>-C<sub>3</sub>N<sub>4</sub> exhibits a two-dimensional morphology without any distinguishable clusters, as shown in Fig. 1b and Fig. S1.† The results of elemental mapping indicate the uniform dispersion of Co species on g-C<sub>3</sub>N<sub>4</sub> (Fig. 1c). The XRD pattern for Co<sub>1</sub>-C<sub>3</sub>N<sub>4</sub> also shows no peaks other than those corresponding to g-C<sub>3</sub>N<sub>4</sub> (Fig. S2<sup>†</sup>). The atomic dispersion of Co sites was further verified by using a HAADF-STEM image, in which the bright spots represent Co atoms and no aggregation of the bright spots was observed (Fig. 1d).<sup>28</sup> The line-scan profiles also confirm that the Co atoms are well isolated (Fig. S3<sup>†</sup>). ICP-MS was employed to determine the actual loading of Co. As listed in Table S1,† the mass loading of Co is 0.07% for Co<sub>1</sub>-C<sub>3</sub>N<sub>4</sub>. A sample comprising CoO nanoparticles on g-C<sub>3</sub>N<sub>4</sub> was also prepared, with a Co mass loading of 0.81% (denoted as CoNP-C<sub>3</sub>N<sub>4</sub>, Fig. S4<sup>†</sup>). SEM and TEM images (Fig. 1e and Fig. S5<sup>†</sup>) show that the  $\alpha$ -Fe<sub>2</sub>O<sub>3</sub> nanorods grown on fluorine-doped tin oxide (FTO) glass have an average length of ~500 nm and an average diameter of ~50 nm. The HRTEM image (Fig. 1f) displays lattice fringes with a lattice spacing of 0.25 nm, which can be assigned to the (110) planes of crystalline  $\alpha$ -Fe<sub>2</sub>O<sub>3</sub>. The top view for the composite photocatalyst clearly shows that the α-Fe<sub>2</sub>O<sub>3</sub> nanorod arrays are covered by highly corrugated Co<sub>1</sub>-C<sub>3</sub>N<sub>4</sub> nanosheets (Fig. S6<sup>†</sup>). Fourier-transform infrared spectrum for Co1-C3N4 shows a series of characteristic peaks of g-C<sub>3</sub>N<sub>4</sub> as those reported in the literature (Fig. 1g). Notably, the peak at 806 cm<sup>-1</sup>, which is assigned to the breathing mode of the triazine unit in carbon nitride, is blue-shifted to 808 cm<sup>-1</sup> when  $Co_1$ - $C_3N_4$  is integrated with  $\alpha$ -Fe<sub>2</sub>O<sub>3</sub> nanorods.<sup>29</sup> Similar shifts are also found for the peaks at 1200 to 1650 cm<sup>-1</sup>, which correspond to the stretching vibration modes characteristic of aromatic g-C<sub>3</sub>N<sub>4</sub> heterocycles.<sup>30</sup> The blue shift can be attributed to the charge transfer between  $Co_1-C_3N_4$  and  $\alpha$ -Fe<sub>2</sub>O<sub>3</sub>, which strongly evidences the successful formation of heterojunctions.21

UV-vis diffuse reflectance spectroscopy was employed to explore the light-harvesting ability of the as-prepared photocatalysts (Fig. S7<sup>†</sup>). The absorption edge for  $Co_1$ - $C_3N_4$ @ $\alpha$ -Fe<sub>2</sub> $O_3$ is significantly extended to 700 nm, covering almost the entire visible region. On the basis of the Tauc plots (Fig. S8<sup>†</sup>), the band gaps of the  $\alpha$ -Fe<sub>2</sub>O<sub>3</sub> nanorod and Co<sub>1</sub>-C<sub>3</sub>N<sub>4</sub> were determined to be 2.12 eV and 2.66 eV, respectively. The energy band structures were further resolved by Mott-Schottky plots (Fig. S9<sup>†</sup>). The positive slopes of the Mott-Schottky plots indicate the n-type characteristics for both the  $\alpha$ -Fe<sub>2</sub>O<sub>3</sub> nanorod and  $Co_1$ - $C_3N_4$ .<sup>31</sup> The flat band potentials of  $\alpha$ -Fe<sub>2</sub>O<sub>3</sub> and Co<sub>1</sub>- $C_3N_4$  were calculated to be 0.36 V and -0.94 V versus the normal hydrogen electrode (NHE), respectively. For the n-type semiconductor, the flat band potential is close to the bottom of the conduction band (CB).<sup>31,32</sup> Now we are able to draw a clear band diagram for the composite structure, as shown in Fig. 2c. To validate the Z-scheme route for the photo-induced charge carriers, ESR spectroscopy was employed to detect 'OH

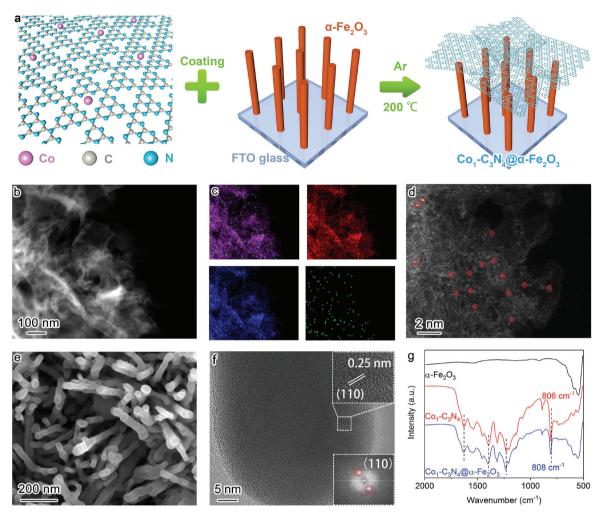


Fig. 1 (a) Schematic illustration of the fabrication strategy for  $Co_1-C_3N_4@\alpha$ -Fe<sub>2</sub>O<sub>3</sub>. (b) Low-resolution HAADF-STEM image for  $Co_1-C_3N_4$  and (c) the corresponding elemental mapping images of C (red), N (blue), and Co (green). (d) Atomic-resolution HAADF-STEM image for  $Co_1-C_3N_4$ . The atomic-ally dispersed Co sites are marked in red circles. (e) SEM image and (f) HRTEM image for the  $\alpha$ -Fe<sub>2</sub>O<sub>3</sub> nanorod arrays; insets: lattice fringes of a single  $\alpha$ -Fe<sub>2</sub>O<sub>3</sub> nanorod (top) and the selected area electron diffraction (SAED) pattern (bottom). (g) Fourier-transform infrared spectra for  $\alpha$ -Fe<sub>2</sub>O<sub>3</sub>,  $Co_1-C_3N_4$ , and  $Co_1-C_3N_4@\alpha$ -Fe<sub>2</sub>O<sub>3</sub>.

and  $O_2^-$  species with DMPO as the trapping agent (Fig. 2a and b). For pristine  $\alpha$ -Fe<sub>2</sub>O<sub>3</sub>, only a weak signal attributed to 'OH was observed under visible-light irradiation; for pristine  $Co_1$ - $C_3N_4$ , only the signal attributed to  $O_2^-$  was detected with four identical peaks. These results are understandable by comparing the energy band positions with the reaction potentials of  $O_2/O_2^-$  and  $H_2O/OH$  (OH<sup>-</sup>/OH). When  $Co_1-C_3N_4@\alpha-Fe_2O_3$ was employed as the photocatalyst, the signals of both 'OH and  $'O_2^-$  were observed with much stronger intensities than that for each single component. In addition, neither of the two species was observed for Co1-C3N4@a-Fe2O3 under dark conditions (Fig. S10<sup>†</sup>), suggesting that the reactive oxygen species mentioned above were generated upon incident light. Therefore, we can conclude that the photo-induced charge carriers follow a Z-scheme mechanism rather than a Type II mechanism (Fig. 2c).8,33

With the Z-scheme mechanism for  $\rm Co_1\text{-}C_3N_4@\alpha\text{-}Fe_2O_3$  validated, now we are in a position to investigate the efficacy of

the composite structure in promoting photocatalytic  $CO_2$ reduction. Fig. 3a shows the average CO evolution rates in CO<sub>2</sub> overall splitting for the as-prepared catalysts under visible light  $(\lambda > 400 \text{ nm})$ . No product was detected for  $\alpha$ -Fe<sub>2</sub>O<sub>3</sub> nanorod arrays, as the potential of the conduction band is too positive to trigger the reduction of CO2. The CO production rate for  $Co_1-C_3N_4(a)\alpha$ -Fe<sub>2</sub>O<sub>3</sub> was substantially elevated to 14.9 µmol g<sup>-1</sup>  $h^{-1}$ , 2.9 times as high as that for Co<sub>1</sub>-C<sub>3</sub>N<sub>4</sub> (5.2 µmol g<sup>-1</sup> h<sup>-1</sup>) and 6.5 times as that for  $C_3N_4@\alpha$ -Fe<sub>2</sub>O<sub>3</sub> (2.3 µmol g<sup>-1</sup> h<sup>-1</sup>). These results imply that the construction of the Z-scheme heterojunction and the introduction of Co favor the photocatalytic reduction of CO<sub>2</sub> under visible light. When ultraviolet light was also introduced to the photocatalytic system (by the removal of the cut-off filter), a CO production rate as high as 25.2  $\mu$ mol g<sup>-1</sup> h<sup>-1</sup> was achieved, demonstrating the excellent CO2 reduction capability for Co1-C3N4@α-Fe2O3 under full spectrum. To evaluate the utilization efficiency of the solar energy, apparent quantum efficiencies (AQEs) for CO gene-

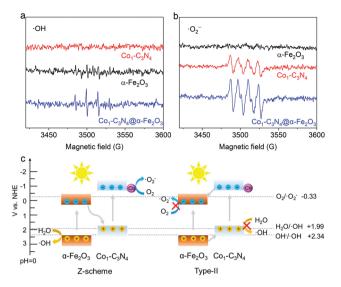
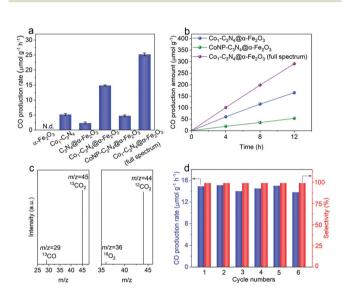


Fig. 2 (a and b) DMPO spin-trapping ESR spectra for  $\alpha$ -Fe<sub>2</sub>O<sub>3</sub>, Co<sub>1</sub>-C<sub>3</sub>N<sub>4</sub>, and Co<sub>1</sub>-C<sub>3</sub>N<sub>4</sub>@ $\alpha$ -Fe<sub>2</sub>O<sub>3</sub> under visible-light irradiation. (c) Schematic illustration for the validation of the Z-scheme mechanism rather than Type-II.



**Fig. 3** (a) CO production rates of  $\alpha$ -Fe<sub>2</sub>O<sub>3</sub>, Co<sub>1</sub>-C<sub>3</sub>N<sub>4</sub>, C<sub>3</sub>N<sub>4</sub>@ $\alpha$ -Fe<sub>2</sub>O<sub>3</sub>, Co<sub>1</sub>-C<sub>3</sub>N<sub>4</sub>@ $\alpha$ -Fe<sub>2</sub>O<sub>3</sub>, and CoNP-C<sub>3</sub>N<sub>4</sub>@ $\alpha$ -Fe<sub>2</sub>O<sub>3</sub>; N.d.: not detected. (b) Time-dependent production of CO by CoNP-C<sub>3</sub>N<sub>4</sub>@ $\alpha$ -Fe<sub>2</sub>O<sub>3</sub> and Co<sub>1</sub>-C<sub>3</sub>N<sub>4</sub>@ $\alpha$ -Fe<sub>2</sub>O<sub>3</sub>. (c) Mass spectra of <sup>13</sup>CO (*m*/*z* = 29) and <sup>18</sup>O<sub>2</sub> (*m*/*z* = 36) produced by Co<sub>1</sub>-C<sub>3</sub>N<sub>4</sub>@ $\alpha$ -Fe<sub>2</sub>O<sub>3</sub> in the isotopic experiments. (d) Cycling production of CO for Co<sub>1</sub>-C<sub>3</sub>N<sub>4</sub>@ $\alpha$ -Fe<sub>2</sub>O<sub>3</sub> in photocatalytic CO<sub>2</sub> reduction with pure water.

ration were determined under different monochromatic light irradiation (Fig. S11<sup>†</sup>). The AQEs at 365 nm and 405 nm were determined to be 0.52% and 0.42%, respectively. In addition, it is noteworthy that neither H<sub>2</sub> nor CH<sub>4</sub> was detected in the gaseous products for a continuous 12-hour photocatalytic test, suggesting the high selectivity for CO (Fig. 3b). To the best of our knowledge, the performance of Co<sub>1</sub>-C<sub>3</sub>N<sub>4</sub>@ $\alpha$ -Fe<sub>2</sub>O<sub>3</sub> here is among the top levels in comparison with other g-C<sub>3</sub>N<sub>4</sub>-based

and single-atomic site catalysts in photocatalytic CO<sub>2</sub> coupled with water oxidation (Table S5<sup>†</sup>). To further examine the essentialness of the single-atomic character of Co in CO<sub>2</sub> reduction, CoNP-C<sub>3</sub>N<sub>4</sub>( $\alpha$ -Fe<sub>2</sub>O<sub>3</sub> was employed for comparison. The result shows that the CO production rate for CoNP-C<sub>3</sub>N<sub>4</sub>@α-Fe<sub>2</sub>O<sub>3</sub> is much lower (4.8  $\mu$ mol g<sup>-1</sup> h<sup>-1</sup>), suggesting the critical role of single-atomic Co sites in photocatalytic CO<sub>2</sub> reduction. A similar irradiation test under Ar atmosphere was conducted on Co1-C3N4@a-Fe2O3, and no CO was detected. To further identify the origin of CO, we traced the carbon source in the reduction process using a <sup>13</sup>C isotopic label. Fig. 3c shows the mass spectrum of CO obtained with <sup>13</sup>CO<sub>2</sub> as a substrate under identical photocatalytic reaction conditions; a distinct <sup>13</sup>CO peak (m/z = 29) was observed, indicating that the CO indeed originates from CO<sub>2</sub>. H<sub>2</sub><sup>18</sup>O, instead of H<sub>2</sub><sup>16</sup>O, was also adopted to verify the water oxidation half-reaction, and a clear  ${}^{18}O_2$  peak (m/z = 36) was observed in the mass spectrum. Moreover, molecular oxygen was detected as the product by liquid-phase oxygen measurement system, further confirming that the CO2 reduction is coupled with water oxidation (Fig. S12<sup>†</sup>). As shown in Fig. 3d and S13,<sup>†</sup> the production rate and selectivity of CO for Co1-C3N4@a-Fe2O3 remained almost unchanged during the six consecutive cycles (4 h each), and no aggregation of Co species appeared after the stability test, validating the excellent stability for the Z-scheme system under visible light.

Given the above results, a question naturally arises: What role does the Z-scheme play in enhancing the photocatalytic CO<sub>2</sub> reduction? In addition to the significantly broadened light-absorption range, the dynamic behaviors of the photoinduced charge carriers are also effectively regulated. The photocurrent responses were recorded under intermittent visible-light irradiation in 0.1 M Na<sub>2</sub>SO<sub>4</sub> aqueous solution (Fig. S14<sup>†</sup>). The photocurrent density for  $Co_1-C_3N_4$  ( $a\alpha$ -Fe<sub>2</sub>O<sub>3</sub> is higher than those for  $\alpha$ -Fe<sub>2</sub>O<sub>3</sub> and Co<sub>1</sub>-C<sub>3</sub>N<sub>4</sub>, suggesting the more efficient photo-induced electron-hole separation for improved CO<sub>2</sub> reduction.<sup>34</sup> Electrochemical impedance spectroscopy (EIS) was conducted to reflect the charge transfer resistance (Fig. S15<sup>†</sup>). The Nyquist plots reveal that Co<sub>1</sub>- $C_3N_4(@\alpha-Fe_2O_3)$  has the lowest charge transfer resistance, which is beneficial for the separation and migration of the photoinduced charge carriers.<sup>24,35</sup> To investigate the lifetime of the electron-hole pairs, we employed PL spectroscopy. As shown in Fig. S16,† the main emission peak located at 442 nm can be ascribed to the inter-band recombination of photo-induced charge carriers. The dramatically quenched PL intensity for Co<sub>1</sub>-C<sub>3</sub>N<sub>4</sub>(a)α-Fe<sub>2</sub>O<sub>3</sub> indicates the faster electron migration and the efficient suppression of the carrier recombination.<sup>29</sup> To gain in-depth information for the carrier dynamics, TRPL decay curves for the as-prepared photocatalysts were recorded. As revealed in Fig. 4a and S17,<sup>†</sup> Co<sub>1</sub>-C<sub>3</sub>N<sub>4</sub>( $\alpha$ -Fe<sub>2</sub>O<sub>3</sub> shows a significantly slower decay kinetics than α-Fe<sub>2</sub>O<sub>3</sub> and Co<sub>1</sub>-C<sub>3</sub>N<sub>4</sub>. The PL lifetimes are listed in Table S2.<sup>†</sup> The shorter lifetime  $\tau_1$ is related to the non-radiative relaxation, and the longer lifetime  $\tau_2$  is attributed to the inter-band recombination of the photo-induced excitons, which mainly contributes to the

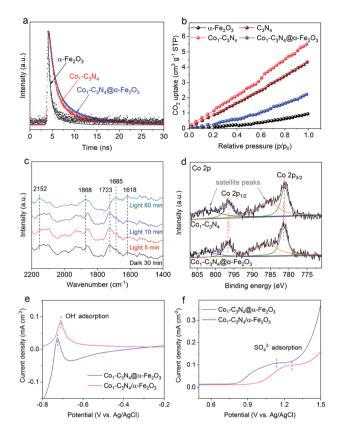


Fig. 4 (a) TRPL decay curves for  $\alpha$ -Fe<sub>2</sub>O<sub>3</sub>, Co<sub>1</sub>-C<sub>3</sub>N<sub>4</sub>, and Co<sub>1</sub>-C<sub>3</sub>N<sub>4</sub>( $\alpha$ -Fe<sub>2</sub>O<sub>3</sub>. (b) CO<sub>2</sub> adsorption isotherms for  $\alpha$ -Fe<sub>2</sub>O<sub>3</sub>, g-C<sub>3</sub>N<sub>4</sub>, Co<sub>1</sub>-C<sub>3</sub>N<sub>4</sub>, and Co<sub>1</sub>-C<sub>3</sub>N<sub>4</sub>( $\alpha$ -Fe<sub>2</sub>O<sub>3</sub>. (c) *In situ* DRIFTS spectra for Co<sub>1</sub>-C<sub>3</sub>N<sub>4</sub>( $\alpha$ -Fe<sub>2</sub>O<sub>3</sub> under different irradiation conditions with the existence of CO<sub>2</sub> and H<sub>2</sub>O. (d) X-ray photoelectron spectroscopy spectra of the Co 2p core levels for Co<sub>1</sub>-C<sub>3</sub>N<sub>4</sub> and Co<sub>1</sub>-C<sub>3</sub>N<sub>4</sub>( $\alpha$ -Fe<sub>2</sub>O<sub>3</sub>. Single oxidative LSV scans at 100 mV s<sup>-1</sup> in (e) Ar-bubbled 0.5 M NaOH and (f) Ar-bubbled 0.1 M Na<sub>2</sub>SO<sub>4</sub> for Co<sub>1</sub>-C<sub>3</sub>N<sub>4</sub>( $\alpha$ -Fe<sub>2</sub>O<sub>3</sub> and Co<sub>1</sub>-C<sub>3</sub>N<sub>4</sub>( $\alpha$ -Fe<sub>2</sub>O<sub>3</sub>, respectively.

photoluminescence.<sup>21</sup> Notably, the average lifetime ( $\tau$ ) of Co<sub>1</sub>-C3N4@a-Fe2O3 is prolonged to 5.17 ns, suggesting the high efficacy of the Z-scheme heterojunction. Specifically, the photo-induced electrons in the conduction band of  $\alpha$ -Fe<sub>2</sub>O<sub>3</sub> can efficiently annihilate the holes in the valence band of Co<sub>1</sub>-C<sub>3</sub>N<sub>4</sub>, thus suppressing the recombination of photo-induced excitons inside each component. As a consequence, more photo-induced electrons would be preserved on the conduction band of Co1-C3N4, and more photo-induced holes would be preserved on the valence band of  $\alpha$ -Fe<sub>2</sub>O<sub>3</sub>, thus leading to superior photocatalytic performances. Furthermore, the incorporation of single-atomic Co sites also results in prolonged average lifetimes with significantly altered  $\tau_1$  and  $\tau_2$ . The atomically dispersed Co can act as effective trap sites to capture the photo-induced electrons from the conduction band of g-C<sub>3</sub>N<sub>4</sub>, thereby inhibiting the recombination of the electrons with the VB holes.<sup>36,37</sup> Therefore, for  $Co_1-C_3N_4(@\alpha-Fe_2O_3)$ , the Z-scheme structure and the single-atomic Co sites collaboratively contribute to the efficient separation of the photo-induced excitons.

To shed light on the role of single-atomic Co sites at the catalytic interface during photocatalytic CO<sub>2</sub> reduction, CO<sub>2</sub> adsorption was employed to determine the chemisorption capacities of these catalysts. As depicted in Fig. 4b, Co<sub>1</sub>-C<sub>3</sub>N<sub>4</sub> adsorbs a much larger amount of CO2 than bare g-C3N4, suggesting the efficacy of the single-atomic Co sites. It is also worth pointing out that the integration of  $\alpha$ -Fe<sub>2</sub>O<sub>3</sub> significantly reduces the CO<sub>2</sub> uptake, which can be attributed to the poor  $CO_2$  adsorption ability of  $\alpha$ -Fe<sub>2</sub>O<sub>3</sub> nanorod arrays. To unravel the possible reaction pathway that occurs on Co<sub>1</sub>- $C_3N_4$  ( $\alpha$ -Fe<sub>2</sub>O<sub>3</sub>, we carried out *in situ* DRIFTS measurements to explore the key intermediates in photocatalytic CO<sub>2</sub> reduction. As illustrated in Fig. 4c, the peaks at 1618  $\text{cm}^{-1}$ , 1723  $\text{cm}^{-1}$ , and 1868 cm<sup>-1</sup> can be assigned to bidentate carbonate  $(b-CO_3^{2-})$ , chelating bridged carbonate  $(c-CO_3^{2-})$ , and multibonded CO (m-CO) on the g-C<sub>3</sub>N<sub>4</sub> substrate, respectively.<sup>38,39</sup> The carbonate species are formed by the interaction of the surface O atoms of g-C<sub>3</sub>N<sub>4</sub> with adsorbed CO<sub>2</sub>.<sup>38</sup> During the 60 min irradiation, the peak intensity of  $b-CO_3^{2-}$  remained unchanged, whereas the peak intensity of c-CO<sub>3</sub><sup>2-</sup> significantly decreased. Meanwhile, an obvious increase was observed in the m-CO peak. These results can be explained by the catalytic effect that c-CO<sub>3</sub><sup>2-</sup> is converted into m-CO during the photocatalytic CO<sub>2</sub> reduction. More importantly, a peak at 2152  $\text{cm}^{-1}$  emerged and the intensity of the peak gradually increased with the irradiation time. This peak can be assigned to the stretching vibration of CO adsorbed on an isolated Co site.<sup>40,41</sup> This result further highlights the key role of the single-atomic Co sites in CO evolution. Moreover, another peak at 1685 cm<sup>-1</sup> attributed to CO<sub>2</sub><sup>-</sup> adsorbed on Co sites was observed, the intensity of which noticeably increased after 60 min irradiation.<sup>38,42</sup> Therefore, it can be inferred that the CO2-to-CO conversion on the isolated Co sites proceeds via the formation of CO<sub>2</sub><sup>-</sup>, which is generally regarded as the ratedetermining step in CO<sub>2</sub> reduction.<sup>4,43-45</sup> The stabilization of  $CO_2^{-}$  has a great impact on the overall performance of the photocatalytic CO2 reduction, and largely depends on the local charge density of the active sites.<sup>46–48</sup> In our Z-scheme heterojunction, the electrons in Co<sub>1</sub>-C<sub>3</sub>N<sub>4</sub> with a relatively high Fermi level would spontaneously migrate to  $\alpha$ -Fe<sub>2</sub>O<sub>3</sub> to eliminate the disparity between the Fermi levels,34 which was verified by XPS analysis in Fig. S18<sup>†</sup> and Fig. 4c. The N 1s spectrum for Co<sub>1</sub>-C<sub>3</sub>N<sub>4</sub> can be deconvoluted into three peaks located at 398.3 eV (C-N=C), 400 eV  $(N-(C)_3)$  and 401.3 eV  $(C-N-H_x)$ , respectively.<sup>13,49</sup> Notably, these peaks shift to higher binding energies after assembly with  $\alpha$ -Fe<sub>2</sub>O<sub>3</sub> (Table S3<sup>†</sup>). Moreover, distinguishable shifts in similar trend were also observed for Co 2p<sub>3/2</sub> peaks (Table S3<sup>†</sup>).<sup>13,50</sup> In contrast, in terms of the binding energy of Fe, the Fe 2p peaks of the Z-scheme heterojunction downshift by 0.2 eV relative to those of pristine  $\alpha$ -Fe<sub>2</sub>O<sub>3</sub> (Fig. S19 and Table S4<sup>†</sup>).<sup>51</sup> This result is indicative of a partial electron transfer from N and Co to Fe, confirming the electron migration direction between the two components.<sup>52,53</sup> Accordingly, the Co species in Co<sub>1</sub>-C<sub>3</sub>N<sub>4</sub>@α-Fe<sub>2</sub>O<sub>3</sub> exhibits a higher oxidation state than that in Co<sub>1</sub>-C<sub>3</sub>N<sub>4</sub>. In this case, the negatively charged CO<sub>2</sub><sup>-</sup> can be better stabilized by the electro-

#### Paper

static interaction with the more positively charged Co sites.<sup>45</sup> To confirm the superiority of Co<sub>1</sub>-C<sub>3</sub>N<sub>4</sub>@α-Fe<sub>2</sub>O<sub>3</sub> in CO<sub>2</sub><sup>-</sup> stabilization, the adsorption of OH<sup>-</sup> and SO<sub>4</sub><sup>2-</sup> (as proper surrogates for  $CO_2^{-}$ ) was conducted.<sup>54-56</sup> In order to eliminate any possible disturbance, we prepared a non-heterojunction mixture comprising  $\alpha$ -Fe<sub>2</sub>O<sub>3</sub> nanorod arrays and Co<sub>1</sub>-C<sub>3</sub>N<sub>4</sub> with the assistance of Nafion solution rather than via the subsequent thermal treatment (denoted as  $Co_1-C_3N_4/\alpha$ -Fe<sub>2</sub>O<sub>3</sub>). The oxidative linear sweep voltammograms (LSV) in NaOH aqueous solution reveal that the potential of OH<sup>-</sup> adsorption for  $Co_1$ - $C_3N_4$  (a) $\alpha$ -Fe<sub>2</sub>O<sub>3</sub> is 19 mV lower than that for  $Co_1$ - $C_3N_4/$  $\alpha$ -Fe<sub>2</sub>O<sub>3</sub> (Fig. 4e). This difference becomes more prominent in the adsorption of  $SO_4^{2-}$ . As shown in Fig. 4f, a potential of 1.14 V vs. Ag/AgCl is required for the adsorption of  $SO_4^{2-}$  on  $Co_1-C_3N_4$  (a) $\alpha$ -Fe<sub>2</sub>O<sub>3</sub>, 120 mV lower than that on  $Co_1-C_3N_4/$  $\alpha$ -Fe<sub>2</sub>O<sub>3</sub> (1.26 V vs. Ag/AgCl). Since the lower potential implies a stronger binding of the anion, these results strongly indicate that the Z-scheme Co<sub>1</sub>-C<sub>3</sub>N<sub>4</sub>@α-Fe<sub>2</sub>O<sub>3</sub> can efficiently stabilize the key intermediate CO<sub>2</sub><sup>-</sup>, thereby facilitating CO evolution.

### Conclusions

In summary, we have constructed a Z-scheme heterojunction of Co1-C3N4@a-Fe2O3 comprising Co1-C3N4 and a-Fe2O3 nanorod arrays for efficient visible-light-driven CO2 reduction coupled with water oxidation. The introduction of the Z-scheme heterojunction into a single-atomic catalyst of Co<sub>1</sub>-C<sub>3</sub>N<sub>4</sub> not only promotes the separation of the photo-induced charge carriers for benefiting CO2 reduction, but also enhances the capability of water oxidation. XPS analysis reveals that the single-atomic Co sites in Co<sub>1</sub>-C<sub>3</sub>N<sub>4</sub> become more positively charged after the formation of the heterojunction, which contributes to the efficient stabilization of CO<sub>2</sub><sup>-</sup> and hence facilitates the CO2 reduction, as verified by the in situ DRIFTS spectra and anion adsorption test. As a result, a CO generation rate of 14.9  $\mu$ mol g<sup>-1</sup> h<sup>-1</sup> with over 99% CO selectivity is achieved under visible-light irradiation using water as an electron source. Our findings here underline the importance of the charge regulation on single-atomic sites by the Z-scheme heterojunction for enhancing catalytic performances, and offer a new approach to developing high-efficiency single-atomic site catalysts for artificial photosynthesis.

### Conflicts of interest

There are no conflicts to declare.

### Acknowledgements

This work was supported by the National Key R&D Program of China (2017YFA0700104), the National Natural Science Foundation of China (21931007, 21905204, 21805207) and 111 Project of China (D17003). *In situ* DRIFTS measurements were performed at the Infrared Spectroscopy and Microspectroscopy Endstation (BL01B) in the National Synchrotron Radiation Laboratory (NSRL) in Hefei, China.

### References

- 1 C. F. Shih, T. Zhang, J. Li and C. Bai, *Joule*, 2018, **2**, 1925–1949.
- 2 O. S. Bushuyev, P. De Luna, C. T. Dinh, L. Tao, G. Saur, J. van de Lagemaat, S. O. Kelley and E. H. Sargent, *Joule*, 2018, 2, 825–832.
- 3 S. C. Roy, O. K. Varghese, M. Paulose and C. A. Grimes, *ACS Nano*, 2010, 4, 1259–1278.
- 4 S. N. Habisreutinger, L. Schmidt-Mende and J. K. Stolarczyk, *Angew. Chem., Int. Ed.*, 2013, **52**, 7372–7408.
- 5 J. Ran, M. Jaroniec and S. Z. Qiao, *Adv. Mater.*, 2018, 30, 1704649.
- 6 J. Di, C. Zhu, M. Ji, M. Duan, R. Long, C. Yan, K. Gu, J. Xiong, Y. She, J. Xia, H. Li and Z. Liu, *Angew. Chem., Int. Ed.*, 2018, 57, 14847–14851.
- 7 X. Li, Y. Sun, J. Xu, Y. Shao, J. Wu, X. Xu, Y. Pan, H. Ju, J. Zhu and Y. Xie, *Nat. Energy*, 2019, 4, 690–699.
- 8 Z. Jiang, W. Wan, H. Li, S. Yuan, H. Zhao and P. K. Wong, *Adv. Mater.*, 2018, **30**, 1706108.
- 9 Y. Jiang, J.-F. Liao, H.-Y. Chen, H.-H. Zhang, J.-Y. Li, X.-D. Wang and D.-B. Kuang, *Chem*, 2020, **6**, 766–780.
- 10 Y. Li, Z. Wang, T. Xia, H. Ju, K. Zhang, R. Long, Q. Xu, C. Wang, L. Song, J. Zhu, J. Jiang and Y. Xiong, *Adv. Mater.*, 2016, **28**, 6959–6965.
- X. Li, W. Bi, L. Zhang, S. Tao, W. Chu, Q. Zhang, Y. Luo, C. Wu and Y. Xie, *Adv. Mater.*, 2016, 28, 2427–2431.
- 12 Y. Cao, S. Chen, Q. Luo, H. Yan, Y. Lin, W. Liu, L. Cao, J. Lu, J. Yang, T. Yao and S. Wei, *Angew. Chem., Int. Ed.*, 2017, 56, 12191–12196.
- 13 W. Liu, L. Cao, W. Cheng, Y. Cao, X. Liu, W. Zhang, X. Mou, L. Jin, X. Zheng, W. Che, Q. Liu, T. Yao and S. Wei, *Angew. Chem., Int. Ed.*, 2017, 56, 9312–9317.
- 14 G. Gao, Y. Jiao, E. R. Waclawik and A. Du, *J. Am. Chem. Soc.*, 2016, **138**, 6292–6297.
- 15 P. Huang, J. Huang, S. A. Pantovich, A. D. Carl, T. G. Fenton, C. A. Caputo, R. L. Grimm, A. I. Frenkel and G. Li, *J. Am. Chem. Soc.*, 2018, **140**, 16042–16047.
- 16 S. Tang, X. Yin, G. Wang, X. Lu and T. Lu, *Nano Res.*, 2019, 12, 457–462.
- 17 X. Wang, K. Maeda, A. Thomas, K. Takanabe, G. Xin, J. M. Carlsson, K. Domen and M. Antonietti, *Nat. Mater.*, 2009, 8, 76–80.
- 18 J. Zhang, X. Chen, K. Takanabe, K. Maeda, K. Domen, J. D. Epping, X. Fu, M. Antonietti and X. Wang, Angew. Chem., Int. Ed., 2010, 49, 441–444.
- 19 J. Zhang, J. Sun, K. Maeda, K. Domen, P. Liu, M. Antonietti, X. Fu and X. Wang, *Energy Environ. Sci.*, 2011, 4, 675–678.
- 20 W.-J. Ong, L.-L. Tan, Y. H. Ng, S.-T. Yong and S.-P. Chai, *Chem. Rev.*, 2016, **116**, 7159–7329.

- 21 Z. Zhang, J. Huang, Y. Fang, M. Zhang, K. Liu and B. Dong, *Adv. Mater.*, 2017, **29**, 1606688.
- 22 Y. Wang, H. Suzuki, J. Xie, O. Tomita, D. J. Martin, M. Higashi, D. Kong, R. Abe and J. Tang, *Chem. Rev.*, 2018, 118, 5201–5241.
- 23 Y.-F. Mu, W. Zhang, G.-X. Dong, K. Su, M. Zhang and T.-B. Lu, *Small*, 2020, **16**, 2002140.
- 24 P. Kuang, L. Zhang, B. Cheng and J. Yu, *Appl. Catal.*, *B*, 2017, **218**, 570–580.
- 25 S.-S. Yi, J.-M. Yan and Q. Jiang, J. Mater. Chem. A, 2018, 6, 9839–9845.
- 26 S. Cao, H. Li, T. Tong, H.-C. Chen, A. Yu, J. Yu and H. M. Chen, *Adv. Funct. Mater.*, 2018, **28**, 1802169.
- 27 C. Hu, X. Wang, Z. Qi and C. Li, *Infrared Phys. Technol.*, 2020, **105**, 103200.
- 28 P. Huang, M. Cheng, H. Zhang, M. Zuo, C. Xiao and Y. Xie, *Nano Energy*, 2019, **61**, 428–434.
- 29 X. She, J. Wu, H. Xu, J. Zhong, Y. Wang, Y. Song, K. Nie, Y. Liu, Y. Yang, M.-T. F. Rodrigues, R. Vajtai, J. Lou, D. Du, H. Li and P. M. Ajayan, *Adv. Energy Mater.*, 2017, 7, 1700025.
- 30 M. J. Bojdys, J.-O. Müller, M. Antonietti and A. Thomas, *Chem. - Eur. J.*, 2008, 14, 8177–8182.
- 31 M. Shi, G. Li, J. Li, X. Jin, X. Tao, B. Zeng, E. A. Pidko, R. Li and C. Li, *Angew. Chem.*, 2020, **59**, 6590–6595.
- 32 Y. Zhou, L. Zhang and W. Wang, *Nat. Commun.*, 2019, **10**, 506.
- 33 S. Cao, J. Low, J. Yu and M. Jaroniec, *Adv. Mater.*, 2015, 27, 2150–2176.
- 34 S. Bai, J. Jiang, Q. Zhang and Y. Xiong, *Chem. Soc. Rev.*, 2015, 44, 2893–2939.
- 35 Y. Li, S. Chen, D. Xi, Y. Bo, R. Long, C. Wang, L. Song and Y. Xiong, *Small*, 2018, 14, 1702109.
- 36 Y. Yang, F. Li, J. Chen, J. Fan and Q. Xiang, *ChemSusChem*, 2020, 13, 1979–1985.
- S. Ji, Y. Qu, T. Wang, Y. Chen, G. Wang, X. Li, J. Dong, Q. Chen, W. Zhang, Z. Zhang, S. Liang, R. Yu, Y. Wang, D. Wang and Y. Li, *Angew. Chem.*, 2020, 59, 10651–10657.
- 38 L. Liu, Y. Jiang, H. Zhao, J. Chen, J. Cheng, K. Yang and Y. Li, ACS Catal., 2016, 6, 1097–1108.
- 39 Q.-S. Chen, S.-G. Sun, Z.-Y. Zhou, Y.-X. Chen and S.-B. Deng, *Phys. Chem. Chem. Phys.*, 2008, **10**, 3645–3654.

- 40 J. Jansson, A. E. C. Palmqvist, E. Fridell, M. Skoglundh, L. Österlund, P. Thormählen and V. Langer, *J. Catal.*, 2002, 211, 387–397.
- 41 H.-K. Lin, C.-B. Wang, H.-C. Chiu and S.-H. Chien, *Catal. Lett.*, 2003, **86**, 63–68.
- 42 X. Zu, X. Li, W. Liu, Y. Sun, J. Xu, T. Yao, W. Yan, S. Gao, C. Wang, S. Wei and Y. Xie, *Adv. Mater.*, 2019, 31, e1808135.
- 43 Y. Chen, C. W. Li and M. W. Kanan, J. Am. Chem. Soc., 2012, 134, 19969–19972.
- 44 Ş. Neaţu, J. A. Maciá-Agulló, P. Concepción and H. Garcia, J. Am. Chem. Soc., 2014, 136, 15969–15976.
- 45 A. Wuttig, M. Yaguchi, K. Motobayashi, M. Osawa and Y. Surendranath, *Proc. Natl. Acad. Sci. U. S. A.*, 2016, **113**, E4585–E4593.
- 46 I. V. Chernyshova, P. Somasundaran and S. Ponnurangam, *Proc. Natl. Acad. Sci. U. S. A.*, 2018, **115**, E9261–E9270.
- 47 Y. Hori, H. Wakebe, T. Tsukamoto and O. Koga, *Electrochim. Acta*, 1994, **39**, 1833–1839.
- 48 M. R. Singh, J. D. Goodpaster, A. Z. Weber, M. Head-Gordon and A. T. Bell, *Proc. Natl. Acad. Sci. U. S. A.*, 2017, 114, E8812–E8821.
- 49 J. Liu, H. Shi, Q. Shen, C. Guo and G. Zhao, *Green Chem.*, 2017, **19**, 5900–5910.
- 50 Q. Song, J. Li, L. Wang, Y. Qin, L. Pang and H. Liu, J. Catal., 2019, 370, 176–185.
- 51 Q. Xu, B. Zhu, C. Jiang, B. Cheng and J. Yu, Sol. RRL, 2018, 2, 1800006.
- 52 Y.-X. Liu, H.-H. Wang, T.-J. Zhao, B. Zhang, H. Su, Z.-H. Xue, X.-H. Li and J.-S. Chen, *J. Am. Chem. Soc.*, 2018, 141, 38–41.
- 53 B. Jiang, X.-G. Zhang, K. Jiang, D.-Y. Wu and W.-B. Cai, J. Am. Chem. Soc., 2018, 140, 2880–2889.
- 54 A. Salehi-Khojin, H.-R. M. Jhong, B. A. Rosen, W. Zhu, S. Ma, P. J. A. Kenis and R. I. Masel, *J. Phys. Chem. C*, 2013, 117, 1627–1632.
- 55 F. Lei, W. Liu, Y. Sun, J. Xu, K. Liu, L. Liang, T. Yao, B. Pan, S. Wei and Y. Xie, *Nat. Commun.*, 2016, 7, 12697.
- 56 X. Wang, Z. Chen, X. Zhao, T. Yao, W. Chen, R. You, C. Zhao, G. Wu, J. Wang, W. Huang, J. Yang, X. Hong, S. Wei, Y. Wu and Y. Li, *Angew. Chem., Int. Ed.*, 2018, 57, 1944–1948.